Supporting Information for

Multi-technology characterisation of an unusual surface rupturing intraplate earthquake: The ML 5.4 2019 Le Teil event in France

A. Vallage[1], L. Bollinger[1], J. Champenois[1], C. Duverger[1], A. Guilhem Trilla[1], B. Hernandez[1], A. Le Pichon[1], C. Listowski[1], G. Mazet-Roux[1], M. Menager[1,2], B. Pinel-Puysségur[1], and J. Vergoz[1]

[1]CEA, DAM, DIF, F-91297 Arpajon, France.

[2]Université Côte d'Azur, IRD, CNRS, Observatoire de la Côte d'Azur, Géoazur, 250 rue Albert Einstein, 06560 Valbonne, France

Contents of this file

Introduction

This supporting information provides details on the acquisition and the processing of the different datasets presented in the main paper.

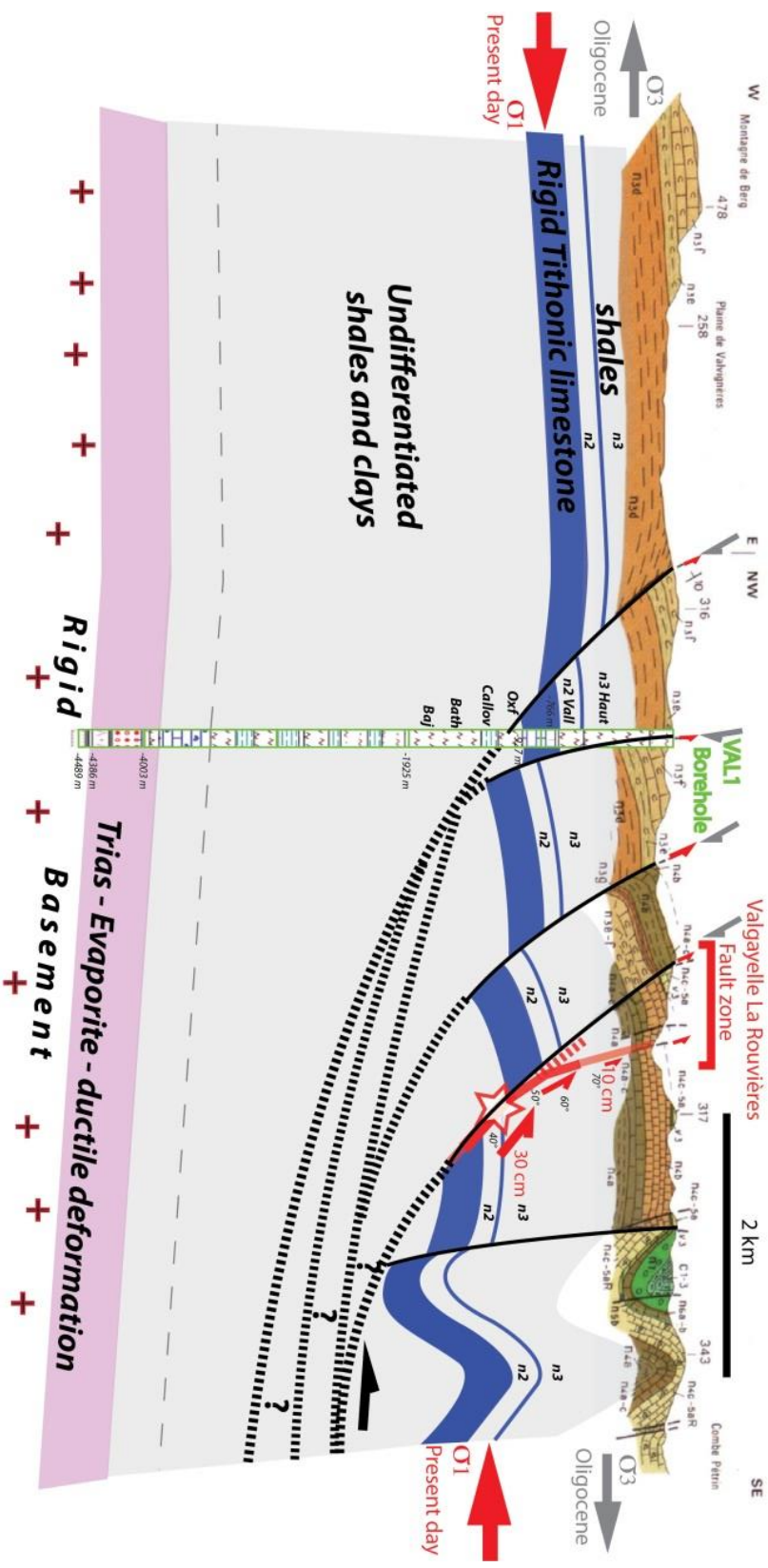

Figure S1. *Zoom on Figure 1 c) in order to allow the reader to better see all the details of the geological cross-section with the Valvignères borehole superimposed.*

Text S1.

Moment tensor inversions and velocity model

Moment tensor inversions are calculated in time domain using TDMT_INVC_ISO (Dreger, 2003). Green's functions are generated using a frequency-wavenumber integration method with FKRPROG (Saikia et al., 1994). We use a 1-D velocity model composed of three layers (Veinante-Delhaye and Santoire, 1980). This velocity model, called LDG model, was derived from arrival times of regional phases (Pg, Pn, Sg and Sn phases) of seismic events well located measured at the CEA seismic stations. It shows a thin (0.9 km) sedimentary layer above a thick crust and a MOHO discontinuity at 25.9 km depth. Such simple model is sufficient to model the wave propagation in France up to several hundred kilometres considering the wavelengths used in the source inversion. It corresponds to the Earth model used for routine seismic event localization at CEA since the end of 1970. The Le Teil earthquake was located using this model for both its automatic location and its revised location.

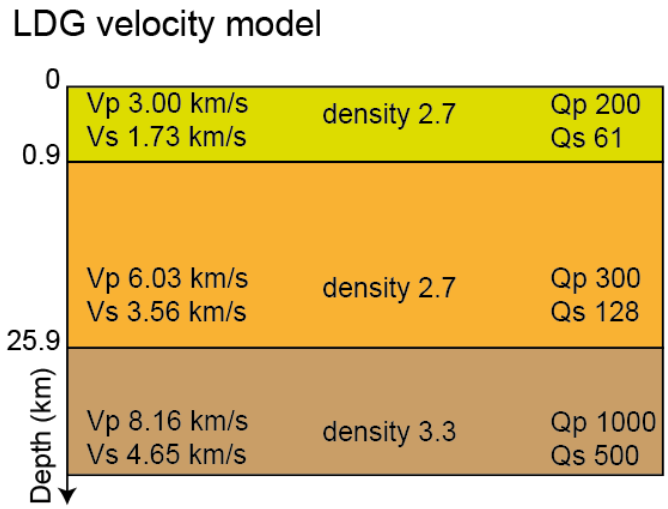

Figure S2. *LDG 1-D velocity model used for seismic event locations and moment tensor analysis at the CEA.*

Uncertainties in the moment tensor solution

In order to estimate the uncertainties in the moment tensor solution using the 10 seismic stations, a jackknife test is performed (Figure S3). Such approach helps to highlight the potential effect of missing stations in the inversion. It was done by successively removing one, two, and three stations out of the poll of 10 stations. Figure S3 shows that the solutions are very stable both in terms of focal mechanism, magnitude and fits. The main divergences are found when stations ARBF and RUSF are not considered (Figure 3). These two stations are required in order to keep a correct azimuthal coverage – these two stations are located in the south-eastern quadrant of the event's radiation pattern.

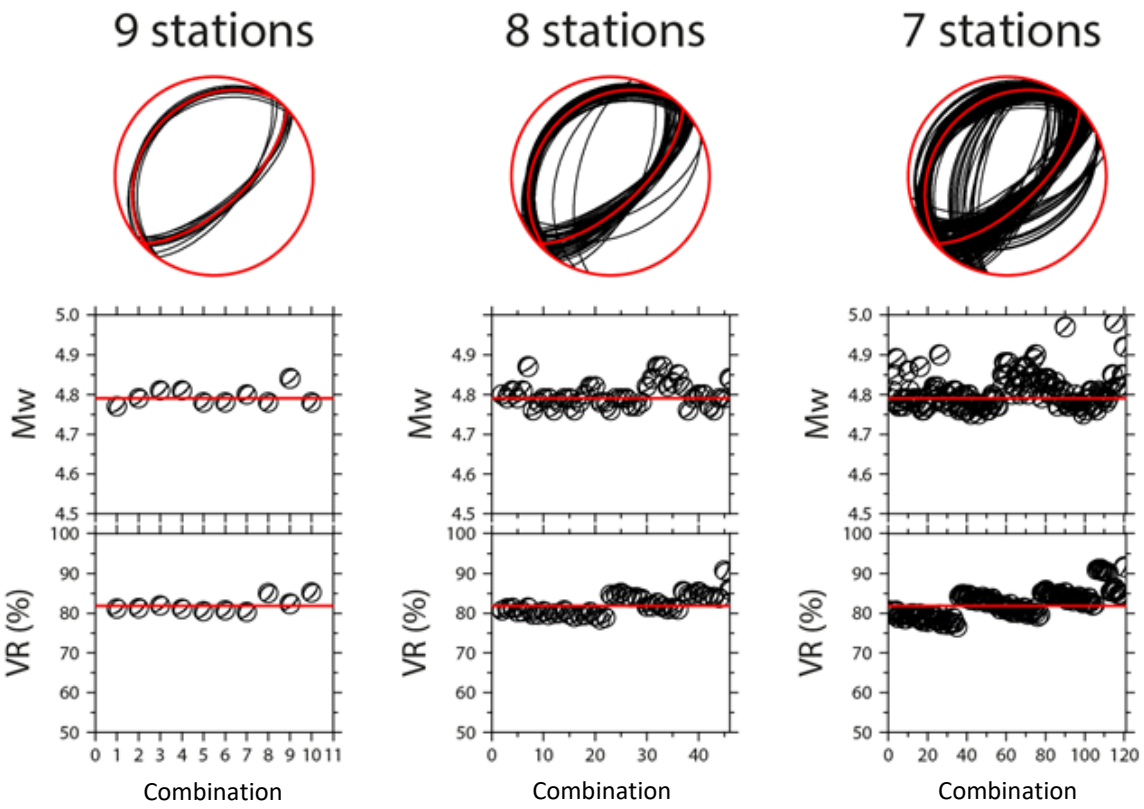

Figure S3. *Jackknife test solutions showing the stability of the moment tensor inversion in terms of focal mechanisms, moment magnitude (Mw) and variance reduction (VR) when 9 (left), 8 (middle), and 7 (right) stations out of 10 are used. The solution obtained using the entire pool of data (10 stations) is shown in red. The horizontal axes show the number of combinations used for each case.*

The uncertainties in the focal mechanism and the magnitude Mw revealed by the Jackknife test are given in Table S1. The uncertainties in the strike, dip, and rake values estimated from the jackknife test agree with the strike, dip, and rake values defined with the solution shown in Figure 2. Regarding the magnitude Mw, the uncertainties are found as follow: Mw: 4.8 +/- 0.01, with a standard deviation of 0.05 magnitude unit.

Table S1. *Uncertainties in the focal mechanism and magnitude estimation of the Le Teil earthquake following the Jackknife test. The optimal solution using 10 regional stations is shown in Figure 2.*

	Optimal solution (10 stations)	Average (Jackknife)	Standard deviation	Uncertainty (99.5%)
Strike 1 (°)	47	47	11	3
Dip 1 (°)	65	64	8	2
Rake 1 (°)	93	95	14	4
Strike 2 (°)	219	218	13	3
Dip 2 (°)	26	29	11	3
Rake 2 (°)	83	82	20	5
Magnitude	4.79	4.81	0.05	0.01

Moment tensor grid search

The location and source characteristics of Le Teil earthquake are also confirmed when using a grid search approach (Figure S4). Inversions are realized at each point of a grid using the same 10 seismic stations (Figure 3). Grid points are spaced every 0.2° in latitude and longitude, centred on the automatic CEA location, and final grid points are placed every 0.1° within a radius of about 96 km centred on the source. The closer the point is to the source location, the higher the value of the variance reduction is.

The overall best-fitting inversion solution (82.76%) is obtained at the point source 44.52°N/6.65°E, about 2 km south of the revised CEA location (Figure S4). This location is very close to the fault surface rupture (Figure 2). Considering the inverted wavelength and the insignificant VR difference between the best solutions of the grid, the solution is found very stable and helps to confirm the source parameters of the mainshock.

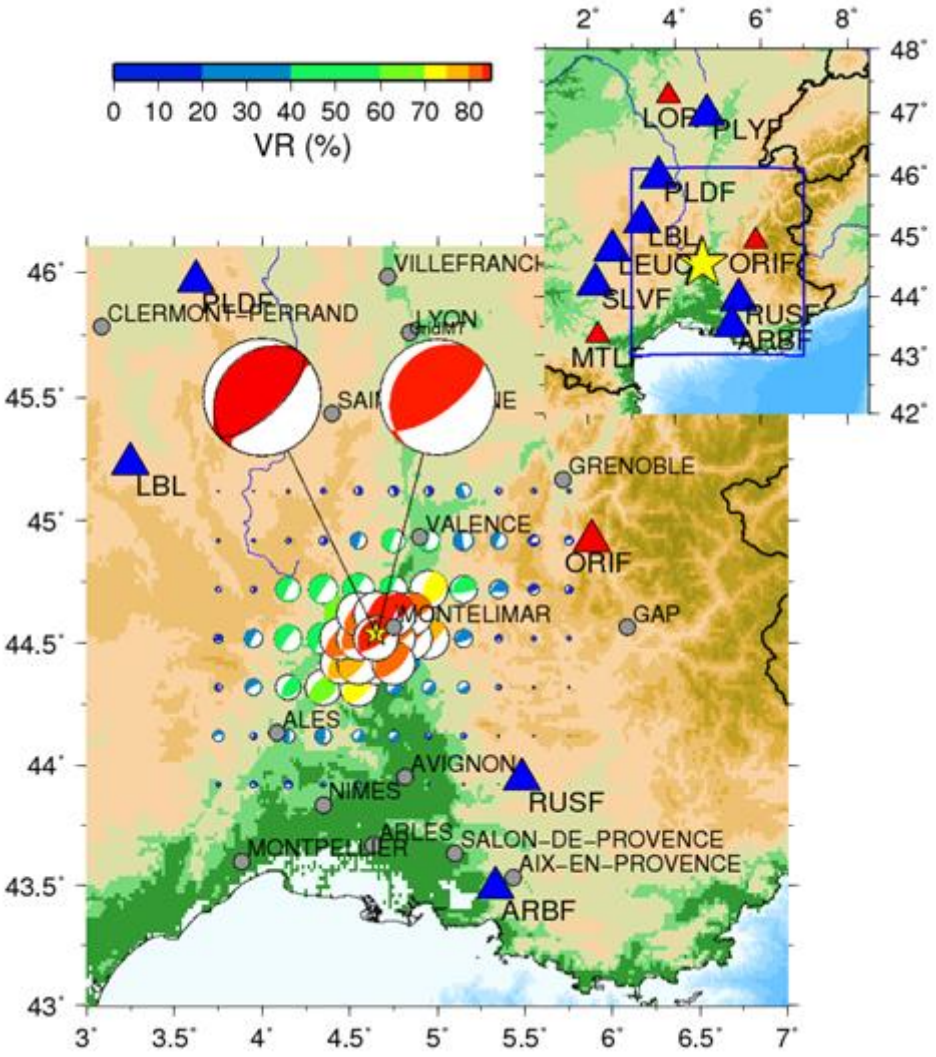

Figure S4. *Moment tensor grid search applied to the Le Teil earthquake. The yellow star shows the revised location. The red triangles show the CEA stations while the RESIF stations are shown by the blue triangles. The beachballs obtained at each point of the grid are color-coded (and sized) by the variance reduction (VR). The point sources are spaced every 0.2° in latitude and longitude and forced at 1 km depth, except within a radius of about 96 km centred on the source where the spacing is 0.1° in latitude and longitude. The best solution of the grid search is found at 0.1° from the source location, with a comparable source mechanism (top right) that the one obtained at the epicentre (top left).*

MS calculation

The surface wave magnitude (MS) is determined using the maximum amplitudes measured at 48 teleseismic stations distributed around the source (Figure S5). The MS is calculated using the approach defined by Vanek et al. (1962) using seismic records filtered around 20 s period. Here, 48 broadband stations between 20° and 90° distance help to estimate a MS of 4.2 +/- 0.3 for Le Teil earthquake.

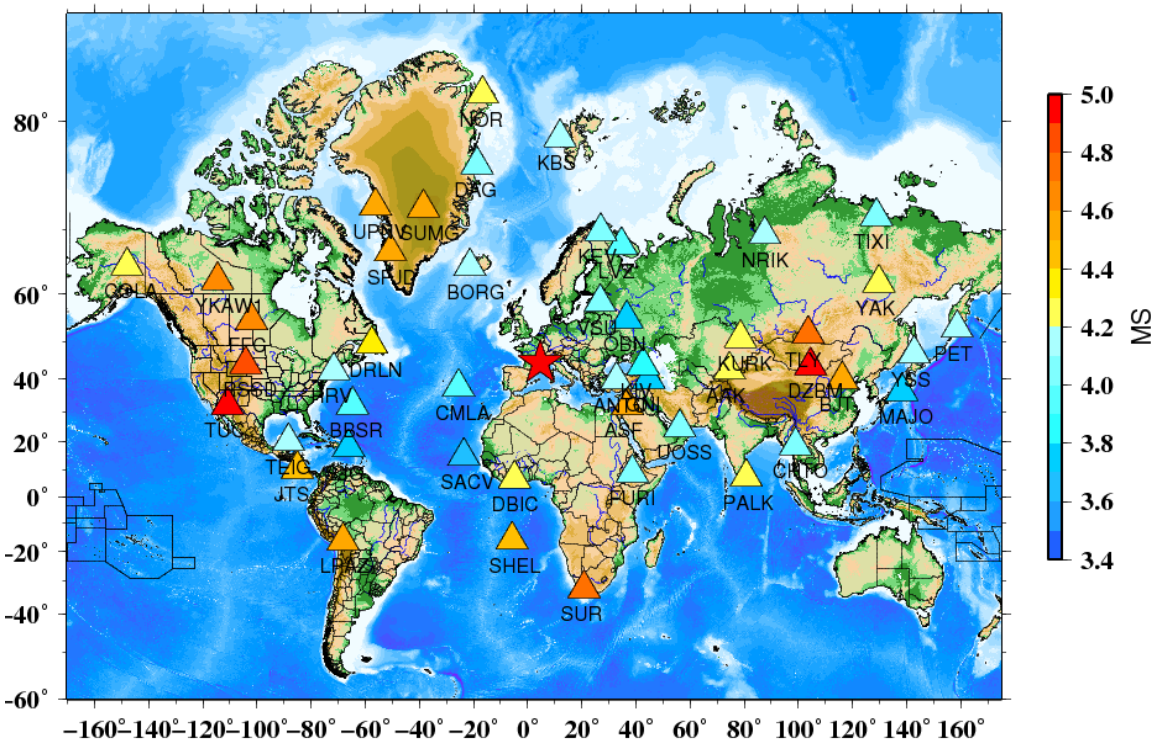

Figure S5. *Map of the 48 broadband seismic stations (triangles) used for the calculation of the surface wave magnitude (MS) of the Le Teil event (red star). The colour of the triangles indicates the MS values measured at each station.*

Figure S5 shows that the determination of the MS is highly dependent of the number of stations used and of their epicentral distance and azimuthal distribution. Indeed, seismic stations located in Europe, and more generally, the closest stations, tend to provide the smallest MS values. On the other side, stations located in the USA, South Africa and in China tend to show the largest values. Figure S6 shows the observed traces on the vertical components for selected stations distributed between 22 and 90°.

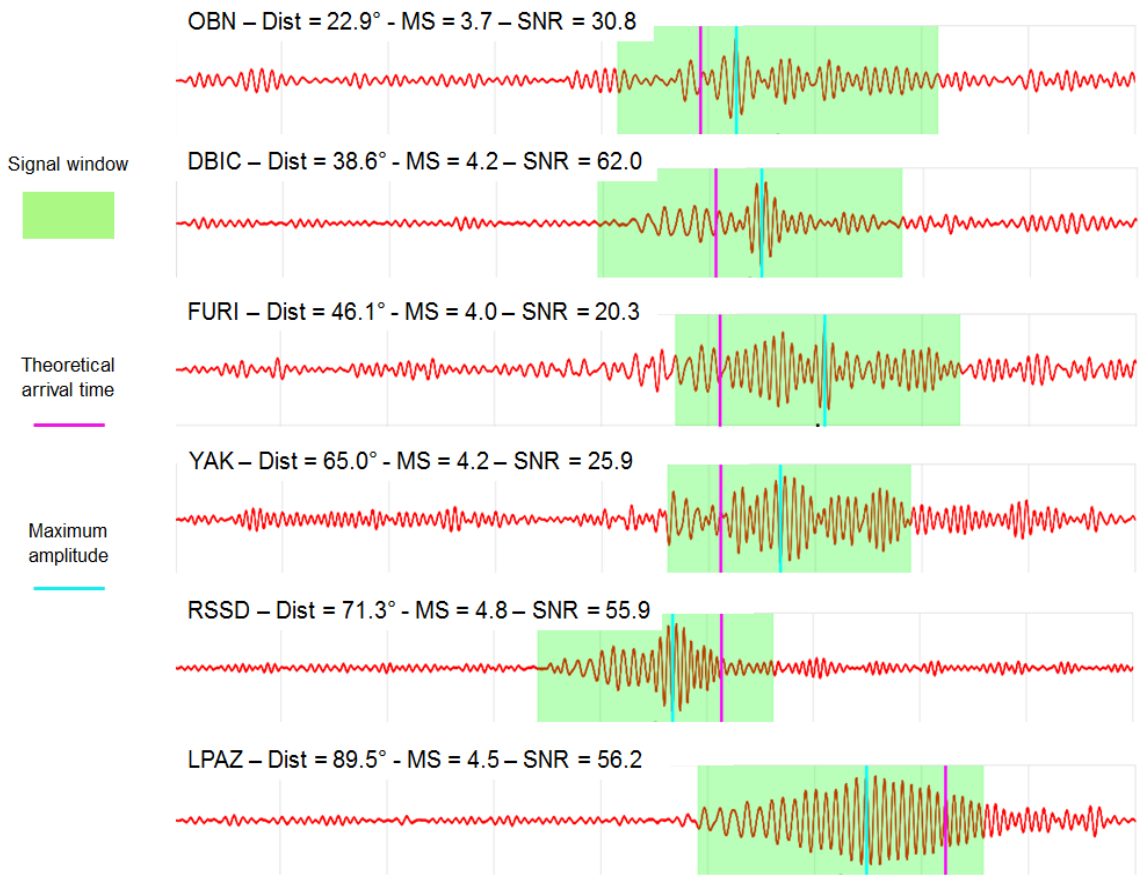

Figure S6. *Selected surface wave records of Le Teil event observed between 22° and 90°. The traces are ordered by epicentral distances. The MS value corresponding to each of them is given. The green area indicates the time period during which, the maximum amplitude is determined. It is based on the 3D velocity model of Ritzwoller and Shapiro (2002). SNR means Signal-to-Noise Ratio.*

Two other MS magnitudes have been calculated using the approach of Russell (2006) and Bonner et al. (2006): these MS magnitudes are called MSVMAX calculated on both Love and Rayleigh waves. Instead of using a limited frequency bandpass window, this method makes use of an increased number of narrow band filters. Here, we use 17 narrow band filters centred on 8 to 40 s period following the data processing given by Guilhem et al. (2015) and Guilhem Trilla and Cano (2017). For the calculation of the MSVMAX values, the same dataset of 48 teleseismic stations is used. After averaging and elimination of outliers, the MSVMAX value based on the Love waves is found equal to 4.3 ± 0.2 from 36 stations, and the MSVMAX value on Rayleigh waves is found 4.4 ± 0.2 from 40 stations.

The three values of MS are in agreement together.

Text S2.

Additional description on InSAR data and inversion.

Sentinel-1 C-band SAR images from two descending and two ascending tracks are used, with different incidence angles (Table S2). Thus, the four coseismic interferograms that have been computed correspond to different lines of sight (Figure S7). They have been processed with the SNAP software (https://step.esa.int/main/toolboxes/snap/). The topographic phase component was removed with the ALOS World 3D-30m digital elevation model (https://www.eorc.jaxa.jp/ALOS/en/aw3d30/) and interferograms were unwrapped using the statistical-cost network-flow phase-unwrapping algorithm SNAPHU (Chen and Zebker, 2001). On the four interferograms, the discontinuity due to deformation close to the surface along the fault trace is clearly visible, with a N45°E azimuth.

All these interferograms are used to invert the displacements on the fault plane following Barnhart and Lohman (2010) and Barnhart et al. (2014). Preliminary, all unwrapped interferograms are downsampled to a computationally tractable number of observations, with three different grid resolutions (1,500 m, 500 m, and 250 m) (Figure S8). We invert the interferograms using an iterative method in which the N45°E fault plane is discretized with triangles whose size is controlled by the model resolution (i.e., smaller patches where finer detail can be resolved) [Barnhart and Lohman, 2010].

For each inversion tests, we fix the strike (N45°E), fault width (4 km), and fault length (7 km) but leave rake free to vary. We use a Laplacian smoothing matrix and choose the optimal smoothing value according to a L-curve criterion (Segall and Harris, 1987). We choose the best fitting model that minimizes the normalized root-mean-square error to the InSAR observations (Figure 4b and S8): it is attained for a dip angle of 60°. The four downsampled interferograms, models and residuals corresponding to this best fit are shown on Figure S8.

Pre event acquisition	Post event acquisition	Relative Orbit	Mode	Polarization	Local incidence angle (°)	Perpendicular baseline (m)	Temporal baseline (days)
06/11/2019	12/11/2019	59	Ascending	VV	43.67	18	6
07/11/2019	13/11/2019	161	Ascending	VV	34.05	92	6
11/11/2019	17/11/2019	37	Descending	VV	35.37	12	6
31/10/2019	12/11/2019	139	Descending	VV	44.73	72	12

Table S2. *Description of the Sentinel-1 interferograms used in this study.*

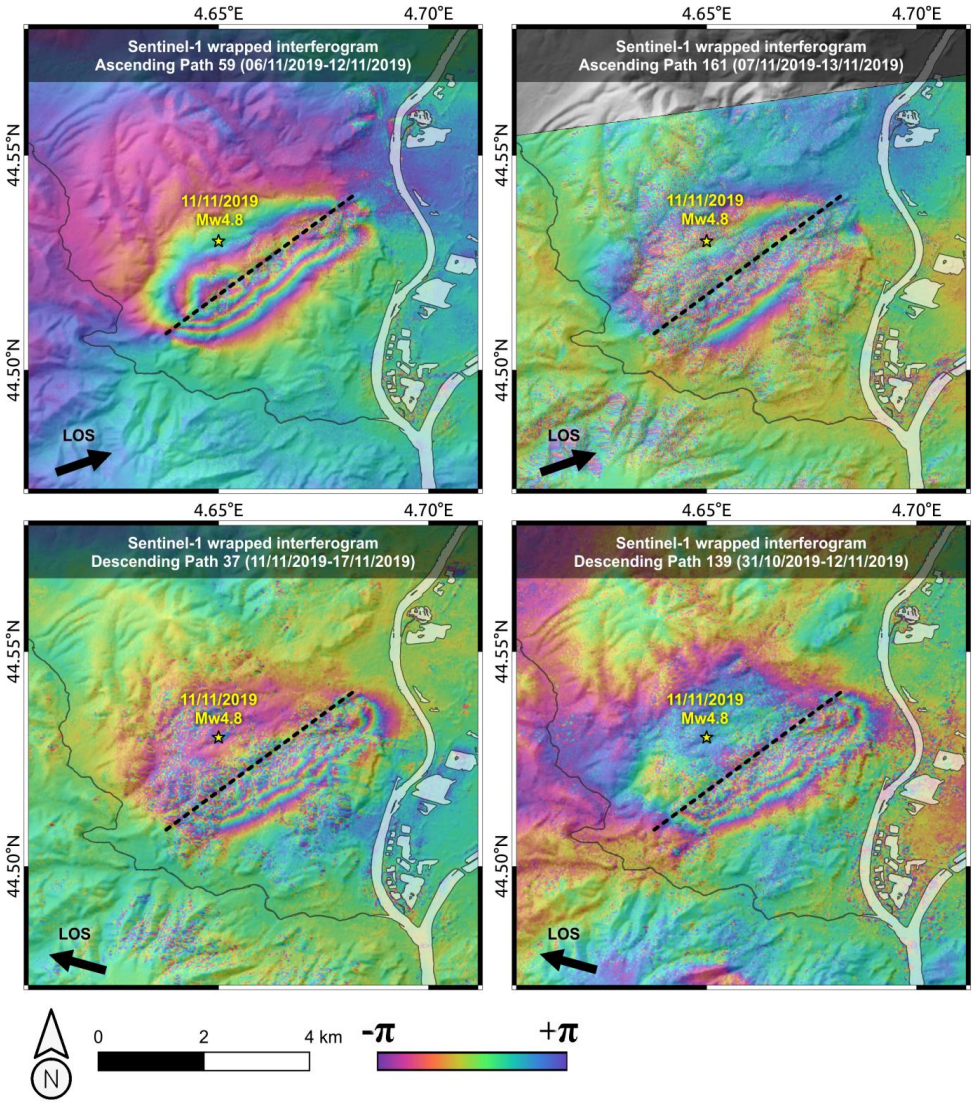

Figure S7. *Sentinel-1 wrapped coseismic interferograms with different look directions. The black dashed line represents the inverted fault surface trace.*

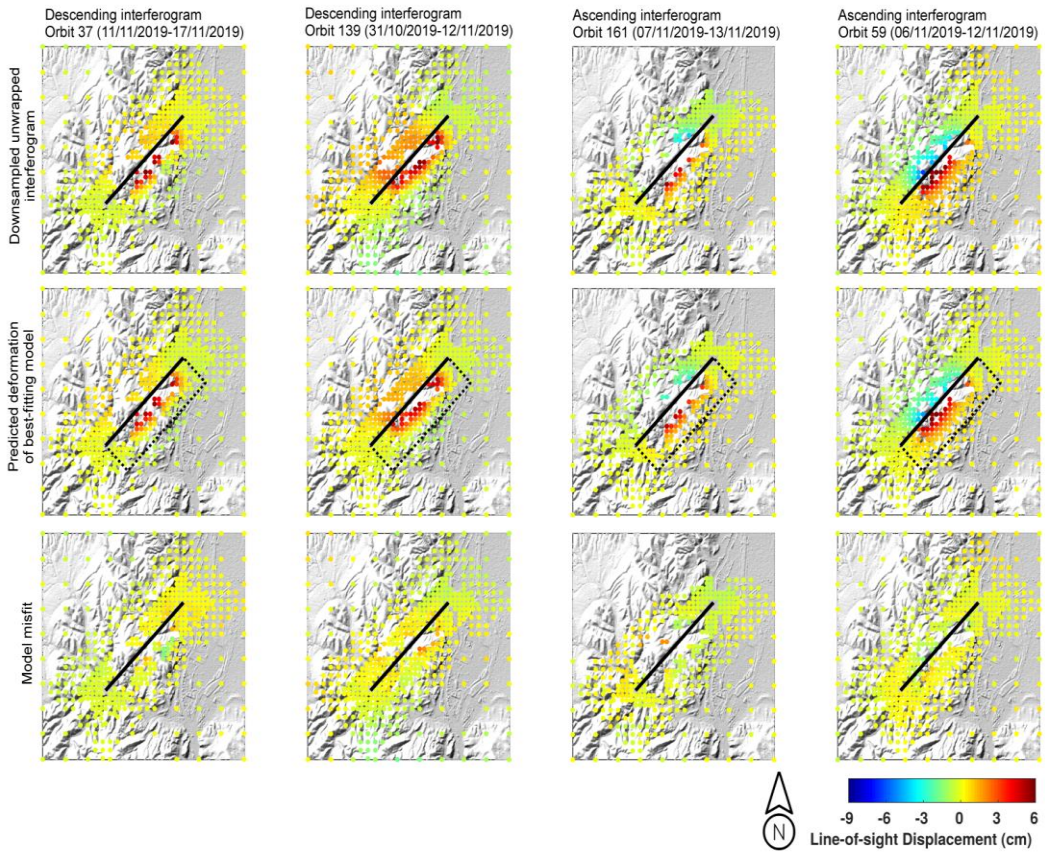

Figure S8. *Downsampled unwrapped interferograms with different look direction, (middle line) synthetics for the best fitting single-fault model, and (bottom line) residuals between data and model. Black box represents the surface projection of the inverted fault geometry.*

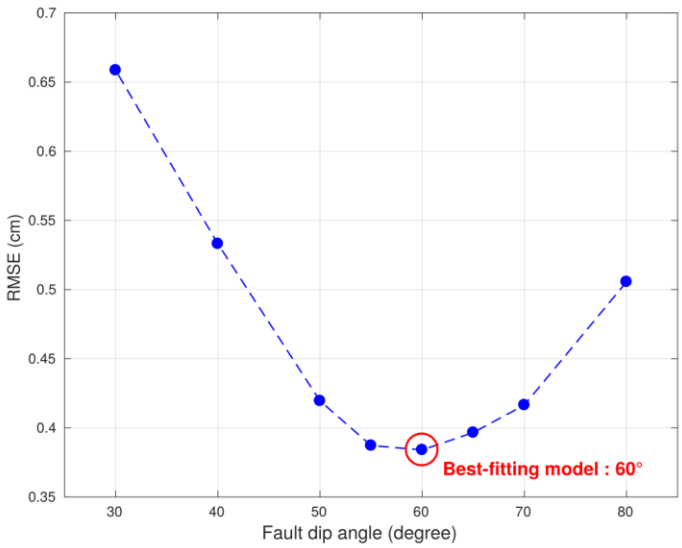

Figure S9. *RMS misfit plot for various fault dip angle models. The red circle shows the best fit dip model shown in the figures 4 and S6.*

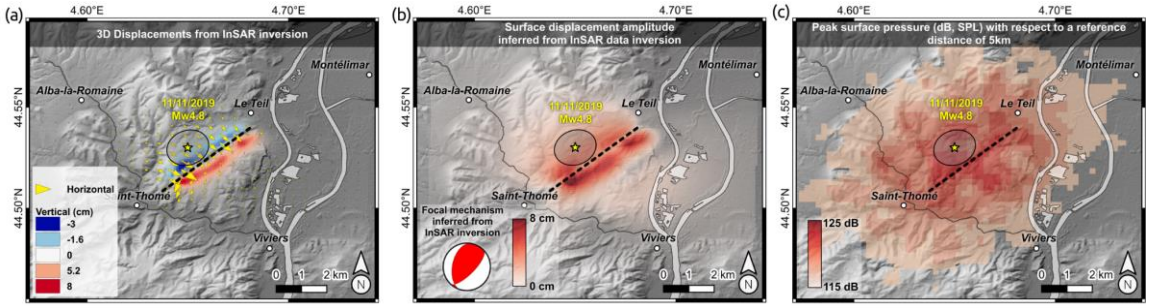

Figure S10. *(a) Vertical displacement amplitude with the horizontal displacement arrows. (b) Absolute displacement (b), compared to the peak surface pressure (PSP) map (c) already shown in Figure 4d.*

Text S3.

Infrasound backprojection method and link between peak surface pressure and peak ground acceleration

We use the inverse location procedure presented in Hernandez et al. (2018), which is based on the following equation:

$$t_d = t_0 + r/V_s + d/V_i$$

where t_0 is the earthquake origin time, r is the propagation range of seismic surface waves traveling at velocity V_s from the epicenter to the area of air-ground coupling where infrasound is emitted, and d is the propagation range from this acoustic source to OHP of stratospherical arrivals with celerity V_i. A constant velocity V_s of 3.3 km/s for seismic surface wave propagation is assumed. Infrasound celerity V_i and azimuthal correction values are derived from paraxial ray-tracing simulations using WASP-3D (Windy Atmospheric Sound Propagation) (Virieux et al., 2004) and ECMWF IFS atmospheric specifications. Eigenrays associated with the measured travel time are modelled by mirroring all simulated upward propagating rays to fall back to OHP following the approach developed by Blixt et al. (2019). These rays correspond to partially reflected ray paths at stratospheric altitude (~30 km) with a celerity of ~300 m/s. Cross-wind effect calculated along the ray paths is about +1°. To account for uncertainties due to the array geometry (Szuberla and Olson, 2004) and propagation effects (Assink et al., 2014), a range of uncertainty of ±1° for the wind-corrected back azimuths and ±5 m/s for the celerity are incorporated in the location procedure, yielding source location errors of ~2 km.

Considering the wavelength of the seismic surface waves (~3 km) at the dominant frequency of the observed infrasound signals (1 Hz), isophase vibration of each source element can be assumed if R_p remains smaller than 1 km. At a large enough observation distance R_0 (set to 5 km for the far field approximation to hold), the Rayleigh integral formulation is applied to compute PSP (Walker et al., 2013). The spatially extended source distribution is modelled by disks R_p radiating energy proportional to the surface motion normal to each vibrating element. Following this approach, PSP (in Pa) is approximated by:

$PSP(x,y) = 31.8\, max\{\|\dot{u}_z(x,y,t)\|\}$

where $\dot{u}_z(x,y,t)$ is the measured vertical acceleration and (x,y) are the coordinates defining the piston surface area across which the acceleration may vary. Note the different coefficient

from Walker et al. (2013), explained by a different choice for the geometry of the source elements (disks instead of squares) and for R_0 (5 km instead of 2.5 km).

Text S4.

Infrasound propagation simulation

Parabolic equation (PE) method is used to simulate the propagation of infrasound waves from the epicentral region to OHP (Figures S11c and S11f, colours). PE method has the advantage of being able to account for diffraction and scattering of acoustic energy into the geometric shadow zone compared with ray tracing technique (grey lines in Figures S11c and S11f). Figures S11a and S11d show the vertical profile of the effective sound speed derived from the ECMWF products (see main text), which defines the possibility for infrasound waveguides to occur when ceff(z)>ceff(z=0). The profile in Figure S11d was modified by adding empirical wind and temperature perturbations of gravity waves (see text S5) in order to be able to explain the infrasound observation at OHP. This technique was already successfully employed with the PE method to explain unexpected explosion detections in the infrasound range across Europe (Green et al. 2010). The average acoustic energy attenuation due to the propagation at 600 m altitude at OHP (~110 km from Le Teil), is represented in Figures S11b and S11e. This attenuation is reduced (by ~5 dB) when adding the gravity wave field.

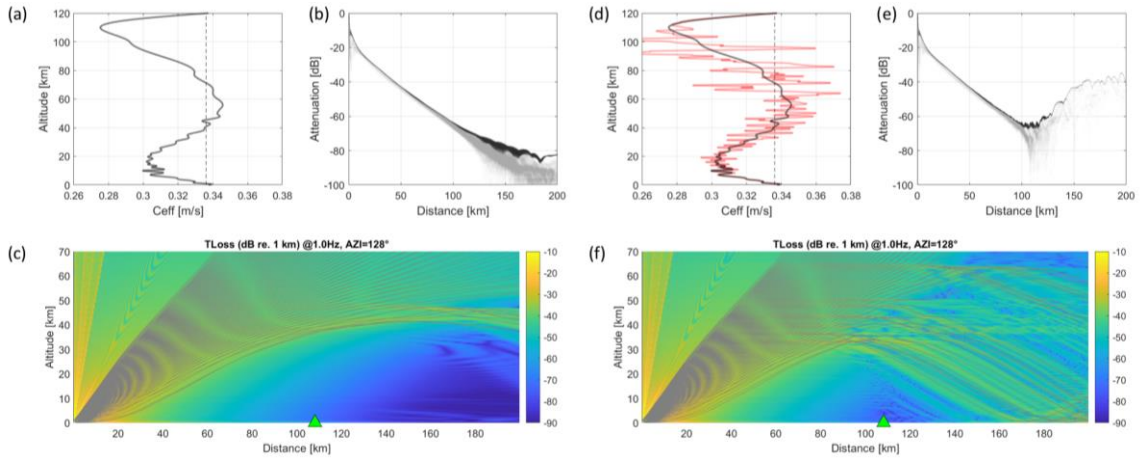

Figure S11. *Parabolic Equation (PE) simulations at 1 Hz to derive the attenuation of the acoustic energy at OHP, ~110 km away from Le Teil (taken at reference of 1 km from the source). (a,d) Vertical profile of the effective sound speed (black solid line) with (a) and without (d) the perturbation by one gravity wave realization (red solid line) of the (modified) Gardner et al. (1993)'s model with perturbation amplitudes multiplied by two (see text S4 for details). The vertical dashed line marks the sound speed at the surface. (b,e) Attenuation of the acoustic energy as a function of the distance to Le Teil corresponding to the meteorology (a) and (d), respectively. Light grey lines represent the predicted attenuation from the ground level to a level of 2 km, with the dark grey lines indicating the maximum amplitude. (c,f) Acoustic energy attenuation through the atmosphere with ray paths superimposed (grey lines). The attenuation is colour coded (in dB) and the OHP station indicated (green triangle).*

The role of gravity waves in explaining infrasound signal detection at OHP, from Le Teil's earthquake is also evidenced through broadband full-waveform modelling (Figure S12), as also done in Green et al. (2010). Normal mode simulations (Bertin et al. 2014; Cugnet et al., 2018) using a set of gravity wave perturbations (Gardner et al. 1993; see text S5) consistent with the one used for the PE method shown in Figure S11. The modelled waveform when gravity waves are accounted for (Figure S12, bottom) is identified as a stratospheric return at about 30 km altitude with a time pick at maximum amplitude close to 300 m/s, consistent with the observation (blue box, at the top) and the ray tracing simulations.

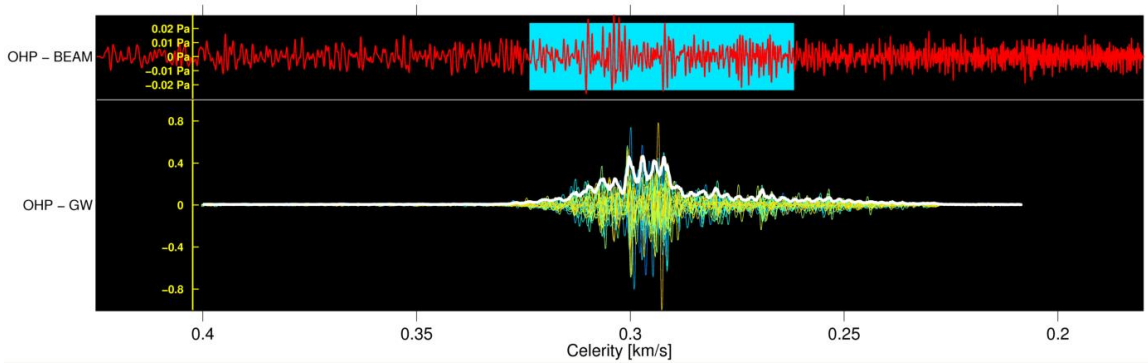

Figure S12. *Modelled infrasound waveforms using normal modes (bottom) with gravity wave perturbations (13 realizations, see text S4) added to the ECMWF wind and temperature profiles. Synthetic signals are compared to that of the observed one (blue box at the top). The x-axis indicates the corresponding celerity values and the y-axis the absolute (top) and normalized (bottom) amplitudes.*

Text S5.

On the gravity wave perturbation

Gravity waves may originate from a wide variety of sources like jets, fronts, wind shear, convection, orography, or geostrophic adjustment (see Fritts and Alexander, 2003, for a review). There are many mountain features between Le Teil and OHP, notably Mont Ventoux (2 km height) at 60 km from Le Teil. Although a more detailed work would be required to state on the exact source of gravity waves needed to explain the infrasound detection at OHP (see text S3), these mountains are likely sources of small-scale propagating temperature and wind perturbations called mountain waves (Fritts and Alexander, 2003). Interestingly, mountain ranges can affect infrasound propagation in different ways. Trapped gravity waves (lee waves) near the surface can significantly affect low-level guiding of infrasound waves (Damiens et al. 2018), and upward propagating waves can cause upper-altitude partial reflections to occur (Kulichkov et al. 2010). Here, we are interested in the latter effect to explain the observed stratospheric return. The ECMWF IFS model cannot resolve the entire spectrum of gravity waves (e.g. Preusse et al. 2014). More particularly, fine scale topography is not resolved, leading to an underestimation of the upward propagating gravity wave amplitudes, or to the absence of gravity waves (Wagner et al. 2017). The spectral gravity wave model used here (Gardner et al. 2013) is implemented in CEA's operational tool for infrasound propagation simulations. It is not specifically tailored for orographic gravity waves. However, this approach allows one to realistically investigate the likely role of gravity waves in the infrasound partial reflections into the shadow zone, where the OHP is, by adding the perturbation to the ECMWF wind and

temperature fields, as done in Green et al. (2010). Note that the amplitude of the modelled gravity waves has to be multiplied by two to simulate an infrasound detection at OHP. In our case, this corresponds to a horizontal wind speed perturbation amplitude of ~10 m/s, which appears consistent with other examples of mountain wave amplitudes in the stratosphere (Wagner et al. 2017) and more generally to the biases recorded for the ECMWF model related to the misrepresentation of small-scale perturbations in the stratosphere (Le Pichon et al. 2005). While further worked is needed to investigate the role of (possibly orographic) gravity waves in the infrasound propagation between Le Teil and OHP, this is beyond the scope of the present study.

Text S6.

Correlation coefficients between infrasound and InSAR data

In order to compare infrasound and displacement amplitude inverted from InSAR data (Figure S9 b), the last map has been resampled to the first one which is less resolved, giving 31x31 measurement points, noted (X_i, Y_i) for i=1, …,N, with N the number of measurement points (here 961).

After compensating a global offset of about 2 km, several correlation coefficients between the data have been computed. First, the classical Pearson correlation coefficient ρ is evaluated as (Pearson, 1895):

$$\rho = \frac{\sum_{i=1}^{N}(X_i - \bar{X})(Y_i - \bar{Y})}{\sqrt{\sum_{i=1}^{N}(X_i - \bar{X})^2} + \sqrt{\sum_{i=1}^{N}(Y_i - \bar{Y})^2}}$$

Where $\bar{X}$ is the mean of the X_i. This coefficient measures the linear correlation between variables.

Then, two other correlation coefficients have been computed namely Spearman's correlation coefficient and Kendall's one. The advantage of these coefficients on Pearson's one is that no assumption is needed on the linear dependency between the variables (Kendall, 1938; Spearman, 1904). Both measure how the first variable monotonically varies with the second variable. To do so, a filter rank is applied on both variables. Spearman's correlation coefficient is defined as Pearson's coefficient computed on the ranks of both series. Kendall's correlation coefficient is defined differently: let us consider the number of couples (X_i, Y_i), (X_j, Y_j) for i=1, …,N and j=1, …,N. The total number of couples is N.(N-1)/2. Among them, M fulfills the condition: ((X_i> X_j) and (Y_i>Y_j)) or ((X_i< X_j) and (Y_i<Y_j)), while L couples fulfil the reverse condition. Kendall's coefficient is generally defined as:

$$\rho_K = \frac{M - L}{N.(N-1)/2}$$

More specific formulas are available in cases of equalities between data points. All three coefficients lie in the interval [-1,1] and value 1 (resp. -1) for perfect positive (resp. negative) correlation and 0 if no correlation is observed.

In the present study, Pearson's correlation values 0.73, Spearman's correlation 0.79 and Kendall's correlation 0.57. For all these correlation coefficients, the null hypothesis of independence between the variables can be rejected with a probability greater than $1\text{-}10^{-7}$, due to the high number of independent samples. Note that the resampling of the InSAR map onto the less resolved infrasound map was necessary to ensure independence between samples. Indeed, resampling the infrasound map onto the more resolved InSAR map would have led to correlated infrasound samples due to oversampling. A confidence interval for Pearson's

correlation has been derived using Fisher's transform and lies in the interval [0.69, 0.72] with a 99% confidence. This derivation is approximate as it assumes that the variables are normally distributed which is obviously not the case for positive variables as here but this approximation is tolerable for a high number of samples, as in this study.

Text S7.

Ground motion propagation, PGA measurement and H/V spatial distribution

Here, we first provide some information on the four GMPEs (Ground Motion Prediction Equations) shown in the main paper, which are appropriated for the French context. The BT03 law is the current GMPE used in the French Safety Rule (RFS 2001-01) for deterministic seismic hazard assessment for nuclear installations. Response spectral attenuation laws are derived from datasets mainly constituted of European strong motion records and a few American records for magnitudes above 6. The Ma04 law of peak horizontal ground acceleration was established for France with earthquakes located in the Alps, the Pyrenees, and the Armorican Massif, and recorded by the CEA/LDG network, with stations settled on stiff bedrock. The DC05 law is a regional stochastic GMPE calibrated using weak-motion records from low-to-moderate seismicity areas and adapted for the French Alps. The Am17 law is an empirical GMPE designed for French applications, taking advantage of the Reference Database for Seismic Ground Motion in Europe (RESORCE-2013: http://resorce-portal.eu/). For small-to-moderate magnitudes, French and Swiss events dominate in the dataset used to constrain the GMPE. Moreover, the authors investigated possible regional features of French data to assess the overall performance of the latter model.

GMPEs	Magnitude	Distance (km)
Ma04	$2.6 \leq ML \leq 5.6$	$5 \leq R_{hypo} \leq 700$
BT03	$4.0 \leq Ms \leq 7.9$	$4 \leq R_{hypo} \leq 330$
Am17	$3.0 \leq Mw \leq 7.6$	$1 \leq R_{epi} \leq 200$
DC15	$3.0 \leq Mw \leq 8.0$	$1 \leq R_{epi} \leq 250$

Table S3. Domains of validity in magnitude and in distance indicated by the authors for the four GMPEs presented in Figure 4. BT03: Berge-Thierry et al. (2003), Ma04: Marin et al. (2004), DC15: Drouet and Cotton (2015) and Am17: Ameri et al. (2017). Ms: surface magnitude, ML: local magnitude, Mw: moment magnitude. R_{hypo}: hypocentral distance, R_{epi}: epicentral distance.

In addition to PGA measurements and comparisons with attenuation laws, we computed the H/V ratios thanks to the 272 three-component stations and by averaging the 2-horizontal PGA measurements (Figure S13). We plot H/V ratios as a function of epicentral distances in log-log scale and we estimate a mean H/V ratio of 1.49 (Figure S13b). This value is extremely close to 3/2, which corresponds to the usual approximation when no horizontal observation is available and an acceptable practice defined in the French Basic Safety Rule (RFS 2001-01) for engineering purpose. It means that for the LDG 1-component stations, we could reasonably approximate the horizontal ground motion at national scale, measuring the vertical component and applying a factor 3/2. However, this first-order simplification needs to be further analysed for the whole frequency range and different locations.

Potential geological and/or regional variation of H/V ratios across the metropolitan France (Figure S13a) cannot be clearly observed in this imposing dataset. No clear trend can be highlighted, and H/V variations rather seem governed by local effects. Further specific analyses would be necessary to discuss this point in more details, which is not in the scope of this paper.

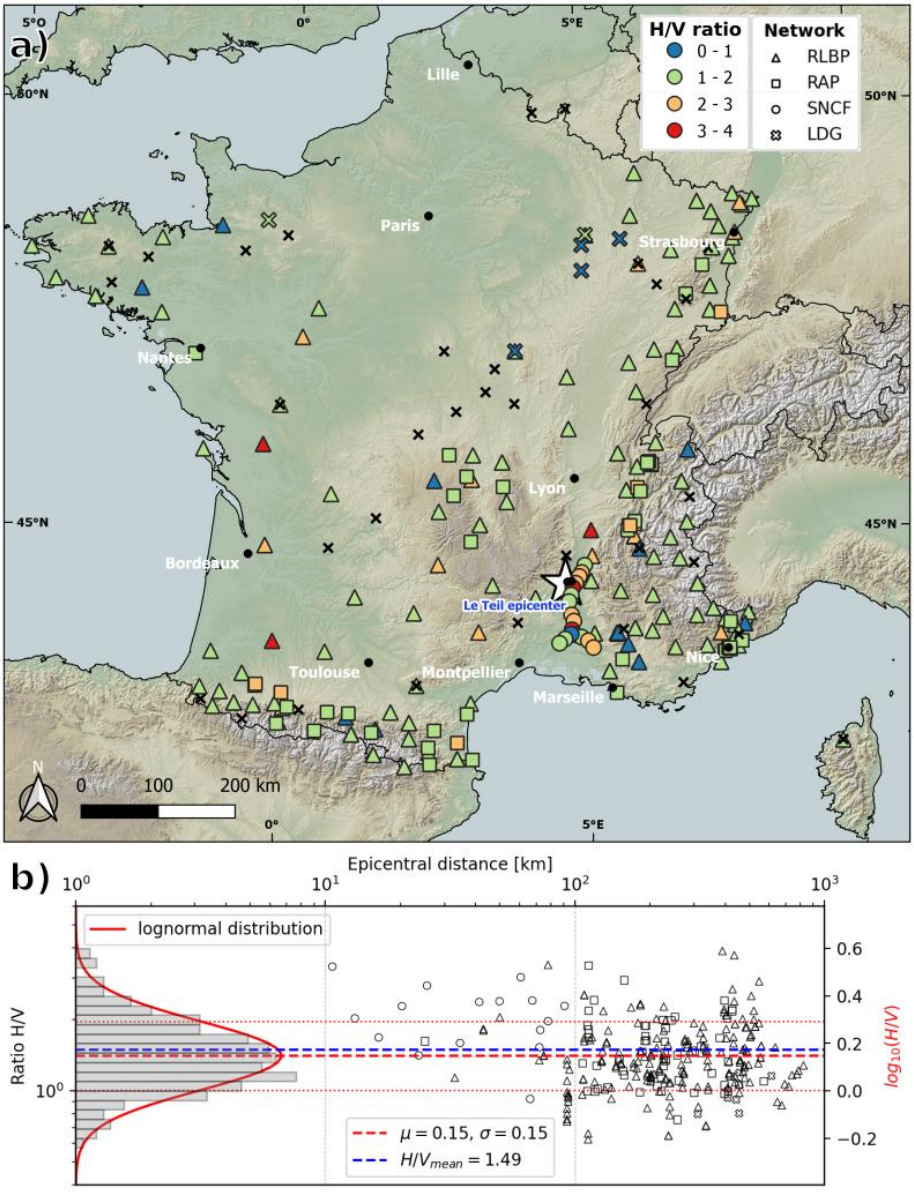

Figure S13. *H/V ratios measured over metropolitan France for Le Teil earthquake. a) Map of H/V ratio per station. Colour is proportional to H/V. b) H/V ratios as a function of epicentral distance in log-log scale. H/V is estimated considering the mean PGA over the 2 horizontal components for all 3-component stations. The mean of H/V ratios is 1.49 (dashed blue line), which is extremely close to 3/2. H/V ratios follow a lognormal distribution (histogram and red curve). The normal distribution fit of the logarithm in base 10 of the data gives μ = 0.15 (dashed red line) and σ = 0.15 (dotted red lines).*